



Electron-donating five-membered heterocyclic modulated electronic states boosting visible-light-driven H₂O₂ production

Tao Gao^a, Chen Yang^a, Yong Zheng^{a,*}, Yi Shen^b, Qiao Wang^a, Long Wang^{a,*}, Run Xu^a, Minghui Lv^a, Mingjin Li^a, Zhonglian Shi^a, Li Wang^a, Xin Ying Kong^c, Liqun Ye^{a,*}

^a College of Materials and Chemical Engineering, Key Laboratory of Inorganic Nonmetallic Crystalline and Energy Conversion Materials, China Three Gorges University, Yichang 443002, China

^b College of Environment, Zhejiang University of Technology, Hangzhou 310032, China

^c School of Chemistry, Chemical Engineering and Biotechnology, Nanyang Technological University, 21 Nanyang Link, Singapore 637371, Singapore

ARTICLE INFO

Keywords:

H₂O₂
Photocatalysis
Pyridyl CMP
Five-membered heterocyclic

ABSTRACT

Pyridyl-conjugated microporous polymers (CMPs) were synthesized and discovered that the catalyst with a five-membered heterocycle could facilitate O₂ reduction and H₂O oxidation into H₂O₂ under photo-irradiation. The electronic state structure of the CMPs was further modulated by incorporating aldehyde-based monomers containing five-membered heterocycles. It was observed that the introduction of an electron-donating thiophene ring (Th-CMP) or a furan ring (Fu-CMP) significantly increased the H₂O₂ production yield. Remarkably, the H₂O₂ yield from Th-CMP in pure water and O₂, without the need for any sacrificial agents, achieved 855 μM h⁻¹, which surpasses most of the reported organic polymer photocatalysts. Mechanism researchs indicated Thiophene groups not only expanded the range for visible light absorption, but also facilitates the separation and migration of charge carriers, thereby providing favorable conditions for H₂O₂ generation. This study presents a promising and innovative direction to designing cost-effective and efficient CMPs for the photocatalytic generation of H₂O₂.

1. Introduction

Hydrogen peroxide (H₂O₂) stands as a promising clean and environmentally friendly oxidizer, which offers a wide range of applications in chemical synthesis, sewage treatment, paper industry, sterilization, and disinfection [1,2]. While the conventional anthraquinone method can produce H₂O₂ efficiently, it involves a complex and energy-intensive multi-step hydrogenation reaction [3–5]. Electrocatalysis presents an alternative route for H₂O₂ production. However, the use of precious metals in electrocatalytic H₂O₂ generation has limited its development [6]. On the contrary, the photocatalytic generation of H₂O₂ from H₂O and O₂ has garnered substantial interest. This method capitalizes on renewable sunlight as a light source, ensuring the entire process is free of pollutant emissions [7]. In photocatalysis, photocatalysts play pivotal and decisive roles in photocatalytic activity. In recent years, organic polymers such as graphitic carbon nitride (g-C₃N₄) [8,9], covalent organic frameworks (COFs) [10,11], covalent triazine frameworks (CTFs) [12], and polymerized resins [13,14] have emerged as potential semiconductor photocatalysts for photocatalytic H₂O₂ production.

CMPs, a class of highly conjugated and stable amorphous porous polymers, has found utility in photocatalytic hydrogen production [15–17], electrochemical energy storage [18], pollutant degradation [19], and even the photocatalytic extraction of uranium [20], but its role in photocatalytic H₂O₂ production remains unexplored. Compared with inorganic photocatalysts such as metal oxides and metal sulfides, CMPs have the advantages of tunable energy band structure and can inhibit the decomposition of H₂O₂. In addition, it can introduce desired chemical groups into its backbone to regulate the visible light absorption range and carrier separation efficiency, thus improving its photocatalytic activity. Comparing with organic photocatalysts such as COF, CMP has the advantages of short synthesis time, can be synthesized in batch, and lower cost. Therefore, CMP has a broad application prospect in the photocatalytic synthesis of H₂O₂.

Donor-acceptor (D-A) polymers excel at light trapping due to their conjugation effect. Polymer photocatalysts with D-A structures has shown effective in bolstering photocatalytic performance [21]. Heteroatom engineering facilitates carrier separation by adjusting push-pull interactions between donors and acceptors, thereby reducing charge

* Corresponding authors.

E-mail addresses: zhengyong@ctgu.edu.cn (Y. Zheng), wanglongchem@ctgu.edu.cn (L. Wang), lqye@ctgu.edu.cn (L. Ye).

<https://doi.org/10.1016/j.apcatb.2024.123761>

Received 26 November 2023; Received in revised form 15 January 2024; Accepted 17 January 2024

Available online 22 January 2024

0926-3373/© 2024 Elsevier B.V. All rights reserved.

recombination. The introduction of a five-membered heterocycle containing a donor electron into the conjugated structure may lead to changes in the electron distribution, which alters photocatalytic properties [22]. In addition, five-membered heterocycles like thiophene, bearing a donor electron, contribute electron density to the conjugated main chain, fostering carrier separation and serving as building blocks for polymers in the field of photocatalysis [23,24]. The integration of such electron-donating five-membered heterocycles into CMP holds promise for enhancing charge carrier separation efficiency and overall photocatalytic activity. We are committed to improving photocatalytic activity by modulating the electronic structures of photocatalysts by designing CMP photocatalysts with broad spectral absorption and high charge separation efficiency.

In this study, we developed pyridyl Ph-CMP via the Chichibabin reaction, then further synthesized pyridyl Th-CMP, enriched with a thiophene ring, by altering the aldehyde monomer (Fig. 1). Our findings disclosed that the introduction of the thiophene ring broadened the visible light absorption range along with band gap alteration, meanwhile effectively improved the wettability and facilitated the adsorption and activation of H_2O and O_2 molecules on the photocatalysts. Comparing with Ph-CMP, the yield of Th-CMP for photocatalytic generation of H_2O_2 in pure water and air, without the addition of any sacrificial agent, was significantly higher, up to $855 \mu\text{M h}^{-1}$, which was 10 times higher than that of Ph-CMP. To investigate the effect of the electron-donating heterocyclic-regulated pyridyl CMP on photocatalytic H_2O_2 production, we also synthesized pyridyl Fu-CMP containing a furan group and compared it with Ph-CMP photocatalyst. We found that the H_2O_2 production rate of Fu-CMP was also significantly higher than that of Ph-CMP. These findings suggest the significance of incorporating electron-giving five-membered heterocycle to modulate the electronic structure of pyridyl CMP to improve its photocatalytic H_2O_2 production activity. More importantly, we found that the electron-rich thiophene moiety in Th-CMP acts as an active site for oxygen reduction, allowing the transfer of received electrons to the adsorbed O_2 molecules and leads to H_2O_2 generation via a two-step single-electron O_2 reduction pathway. Our work shows that the electronic structure of the materials can be tuned by pre-designing the molecular structure to elevate photocatalytic activity. This groundwork strengthens the feasibility of CMPs for practical applications in photocatalytic H_2O_2 generation.

2. Materials and methods

2.1. Synthesis of Ph-CMP

Drug reagents are detailed in the **Supplementary Information**. 1,4-diacetylbenzene (0.32 g, 2 mmol), p-phthalaldehyde (0.13 g, 1 mmol), ammonium acetate (2.31 g, 30 mmol) were added sequentially in a 100 mL round bottom flask, followed by acetic acid (35 mL), and the temperature was maintained at 120°C for 24 h [25]. After the reaction, the solvent was removed by filtration, and the remaining solid was washed with 2% ammonia, ethyl acetate, N, N-dimethylformamide, deionized water, and anhydrous ethanol in sequence. Following that, extraction of solid was performed using methanol, tetrahydrofuran, and acetonitrile for 24 h. Lastly, the precipitates were dried at 60°C for 12 h to obtain yellow powders with 49% yield.

2.2. Synthesis of Th-CMP

1,4-Diacetylbenzene (0.32 g, 2 mmol), thiophene-2,5-dicarboxaldehyde (0.14 g, 1 mmol), and ammonium acetate (2.31 g, 30 mmol) were added sequentially to a 100 mL round bottom flask, followed by the addition of acetic acid (35 mL), and the temperature was maintained at 120°C for 24 h. The remaining steps are the same as for Ph-CMP. Lastly, brown powders with 48% yield were obtained.

2.3. Photocatalytic H_2O_2 production

5 mg catalyst and 10 mL water were evenly dispersed in a quartz bottle with a volume of 50 mL and passed into dry air, stirred for 20 min under dark conditions to reach adsorption-desorption equilibrium, and then irradiated with a xenon lamp source (PLS-SXE300D, Beijing Perfectlight). The samples were collected at every 10 min interval, followed by filtration using a $0.22 \mu\text{m}$ filter before the H_2O_2 content in the solution was quantified [26].

3. Results and discussion

3.1. Structure and morphology

Pyridyl Ph-CMP were synthesized through the polymerization of 1,4-diacetylbenzene and p-phthalaldehyde in the presence of ammonium acetate. To investigate the effect of electron-donating groups in aldehyde-based monomers on the photocatalytic H_2O_2 production

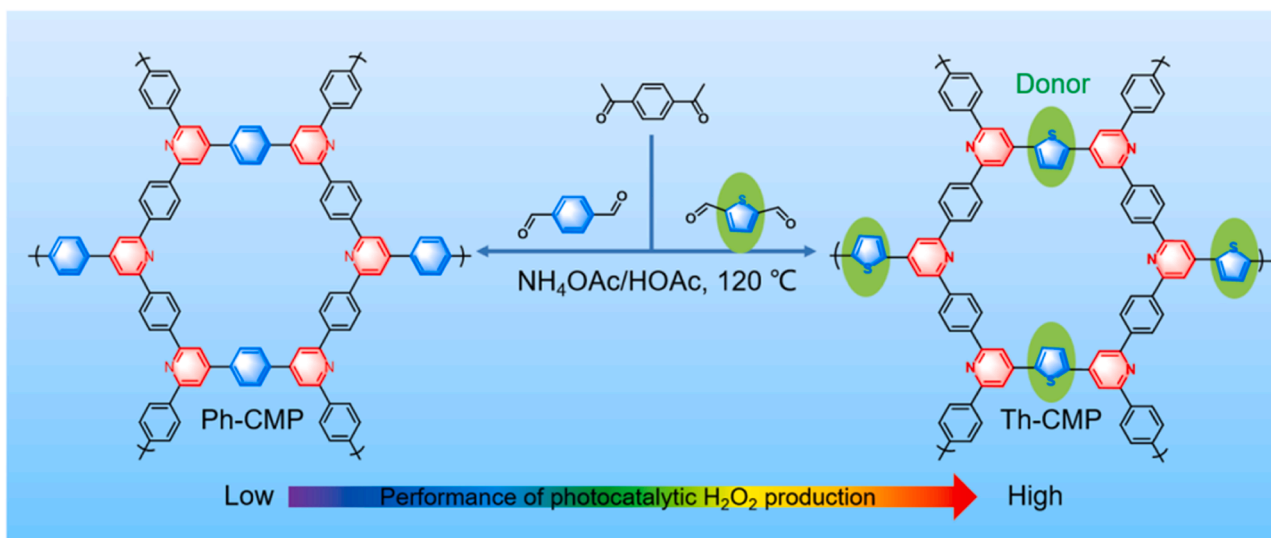


Fig. 1. Schematic diagram for the synthesis of Ph-CMP and Th-CMP.

activity of CMP, Th-CMP with thiophen-ring and Fu-CMP with furan-ring were synthesized using different aldehyde monomers (Fig. 1 and Figure S1). As shown in Fig. 2a and Figure S2a, solid-state ^{13}C cross-polarization/magic angle spin NMR (^{13}C CP/MAS NMR) demonstrated the successful preparation of pyridyl CMP, with three resonance peaks near 140 ppm, 128 ppm, and 25 ppm corresponding to pyridyl, phenyl, and terminal methyl groups, respectively. Resonance peaks at 197 ppm and 189 ppm in Ph-CMP were attributed to the terminal aldehyde and carbonyl groups, respectively [27]. Fourier-transform infrared spectroscopy (FT-IR) disclosed characteristic peaks at 1654 cm^{-1} and 1571 cm^{-1} , attributing to the pyridine ring and benzene ring, respectively (Fig. 2b and Figure S2b) [28]. In addition the characteristic peaks of Th-CMP at 2990 cm^{-1} , a peak at 2892 cm^{-1} was generated by the stretching vibration of the terminal methyl group, whereas the characteristic peak at 1213 cm^{-1} could be attributed to the stretching vibration of C-S-C in the thiophene ring [29]. These findings confirm the completion of the cyclisation reaction.

Powder X-ray diffraction mapping (PXRD) revealed the amorphous nature of all the as-prepared samples (Fig. 2c and Figure S2c). Thermogravimetric analysis (TGA) of Ph-CMP and Th-CMP showed that their decomposition temperatures exceeding 330°C , underscoring the good thermal stability of the synthesized Pyridyl CMP (Figure S3). Field emission scanning electron microscopy (FESEM) and transmission electron microscopy (TEM) showed that Th-CMP is a spherical particle morphology (Figure S4a-c). The elemental mapping disclosed the uniform distribution of C, N, and S elements in the Th-CMP (Figure S4d). From Figs. S5–6, Ph-CMP and Fu-CMP are nanosheet and nanoparticle microstructure, respectively. The elemental mapping of Ph-CMP shows that C and N elements are uniformly distributed.

Survey X-ray photoelectron spectroscopy (XPS) of Th-CMP showed three types of signals at $\sim 163\text{ eV}$, $\sim 285\text{ eV}$, and $\sim 398\text{ eV}$, corresponding to S 2p, C 1s, and N 1s, respectively. Because Ph-CMP does not contain thiophene fraction, the peak of S 2p was not observed (Figure S7). As shown in Fig. 2d, the high-resolution C 1s XPS spectrum

of Th-CMP can be deconvoluted into four peaks centered at 284.8 eV , 285.7 eV , 286.4 eV , and 287.7 eV , corresponding to the C=C bond and C=N bond in pyridine ring, C-S bond in thiophene ring, and the terminal aldehyde or carbonyl group, respectively [30]. In the high-resolution N 1s XPS spectrum, the N 1s peak of Th-CMP can be deconvoluted into two peaks centered at 398.4 eV and 399.9 eV , which are attributable to the C=N and C-N bonds [31] (Fig. 2e). In addition, the high-resolution S 2p XPS spectrum of Th-CMP (Fig. 2f) shows two peaks at S $2p_{3/2}$ (163.9 eV) and S $2p_{1/2}$ (164.9 eV), further verifying the successful synthesis of pyridyl CMP [29]. The N_2 adsorption isotherms reveal that pyridyl CMPs are typical type IV isotherms with mesoporous pore size distribution (Figure S8). Among them, Th-CMP contains three kinds of mesopores (3.1 nm , 4.7 nm , and 7.8 nm), which are larger than the sizes of O_2 and H_2O molecules (about 0.3 nm). It is shown that O_2 and H_2O can diffuse to the surface of the photocatalyst to generate H_2O_2 , and can also react in the interior of the photocatalyst through the pore size. This enhances the activity of photocatalytic generation of H_2O_2 [32]. In addition, based on the contact angle analyses (Figure S9), Th-CMP containing a thiophene ring exhibits a smaller contact angle with water than that of Ph-CMP, indicating that the introduction of the electron-donating thiophene ring increased the hydrophilicity of Th-CMP, which is favourable for the adsorption and activation of O_2 and H_2O .

3.2. Optical and photoelectrochemical properties

Since the energy band positions of photocatalysts are crucial for the generation of H_2O_2 , we systematically investigated the energy band structure of Pyridyl CMP. From UV-vis diffuse reflectance spectra, Th-CMP and Fu-CMP showed stronger absorption in the visible region compared with Ph-CMP, and the absorption edge of Th-CMP was extended to about 800 nm (Fig. 3a and Figure S10a). From Tauc plots, the optical band gaps of Ph-CMP, Th-CMP, and Fu-CMP were estimated to be 2.76 eV , 1.83 eV , and 1.95 eV , respectively (Fig. 3b and

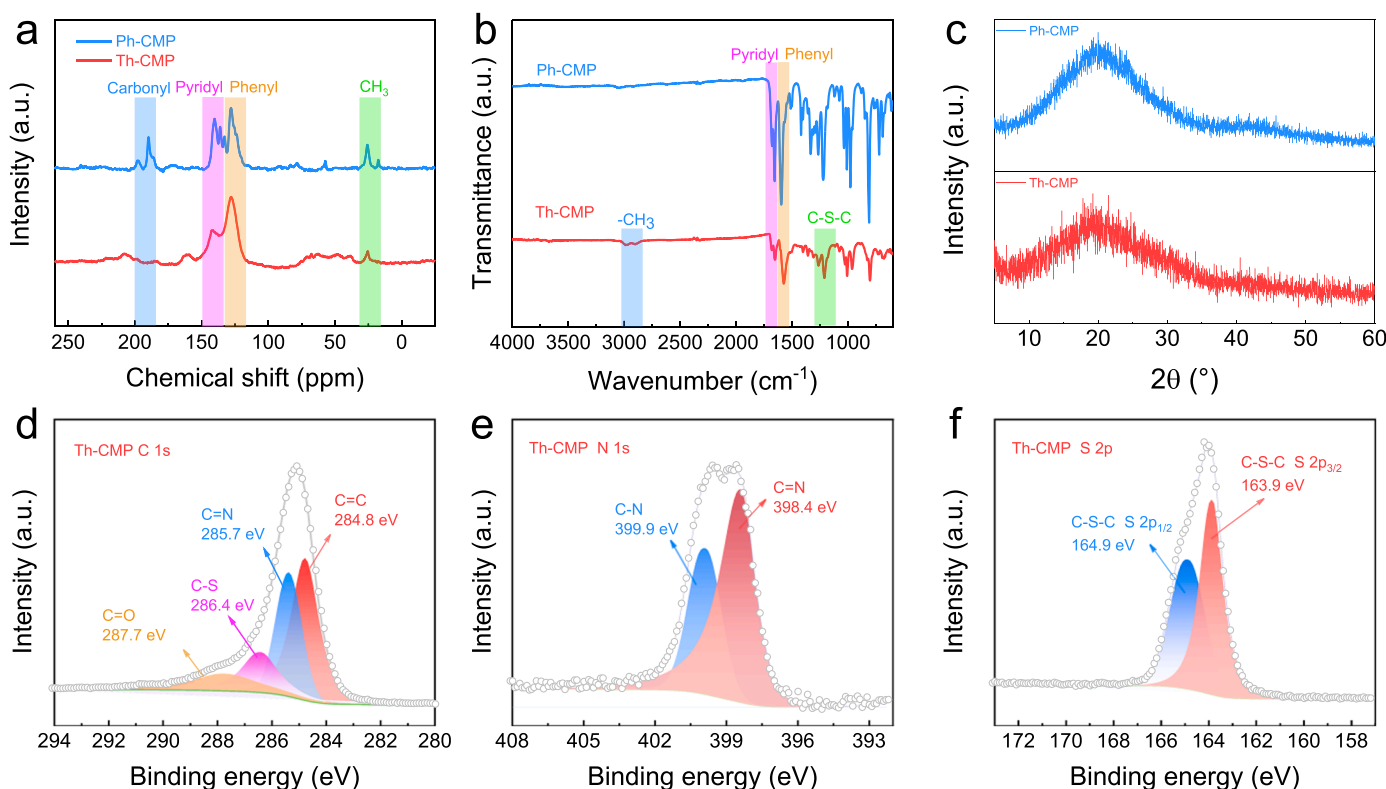


Fig. 2. Structural characterizations. a) Solid-state ^{13}C NMR spectra, b) FT-IR spectra, and c) Powder X-ray diffraction (PXRD) patterns of Ph-CMP and Th-CMP. d-f) High-resolution C 1s, N 1s, and S 2p XPS spectra of Th-CMP.

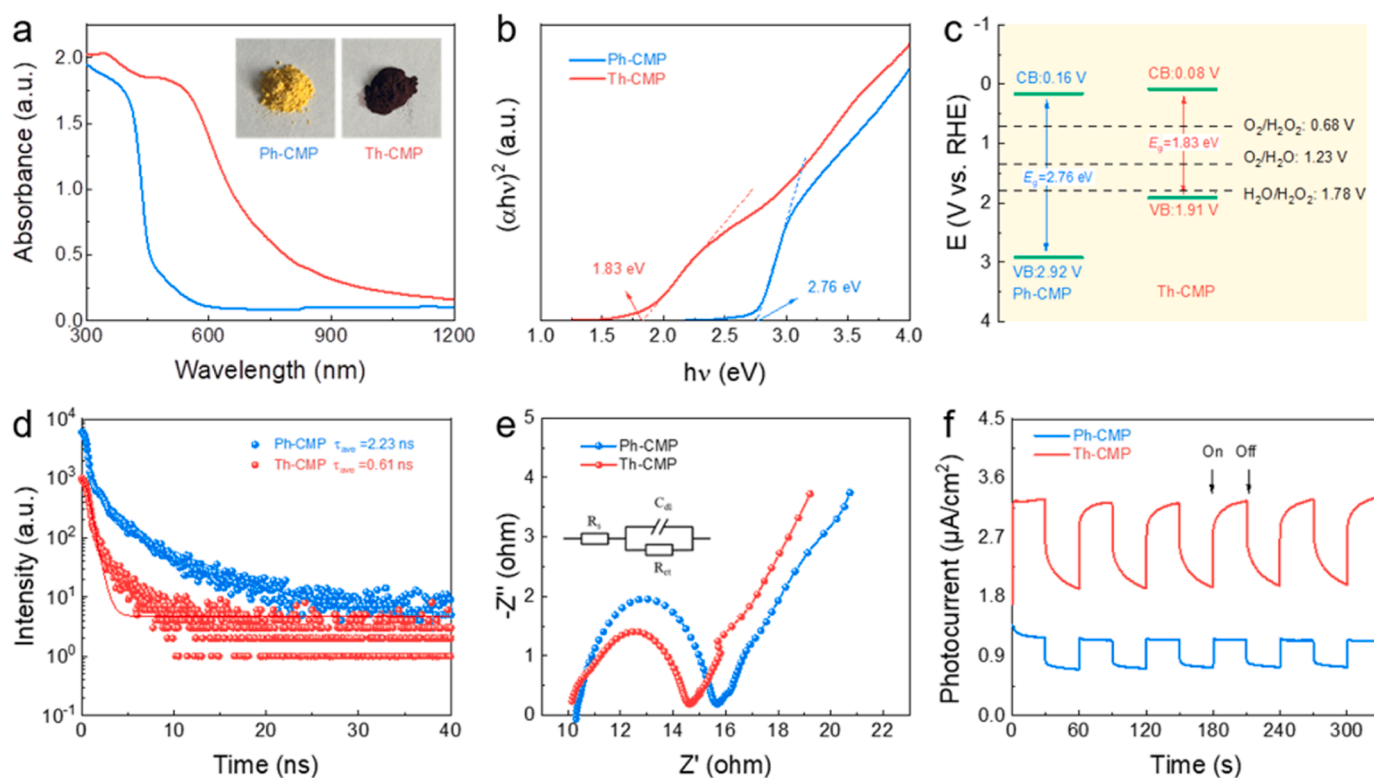


Fig. 3. Optical and photoelectrochemical properties. a) UV-vis DRS spectra, b) Tauc plots, c) schematic diagram for the electronic band structures, d) time-resolved PL decay curves, e) electrochemical impedance spectra (EIS) Nyquist plots, and f) photocurrent responses of Ph-CMP and Th-CMP.

Figure S10b). According to the Mott Schottky plots, the conduction bands of Ph-CMP and Th-CMP are measured as 0.16 V and 0.08 V (vs. RHE), respectively (**Figure S11**). By incorporating with the findings from Tauc plots, the valence band positions of Ph-CMP and Th-CMP are calculated to be 2.92 V and 1.91 V (vs. RHE), respectively [26] (**Fig. 3c** and **Figure S12** show the energy band structures of all pyridyl CMPs and the potentials required to generate H_2O_2 from H_2O and O_2 . Since the conduction band positions of the catalysts are more negative than $E_{\text{H}_2\text{O}_2/\text{O}_2}$ (0.68 V) and the valence band positions are more positive than $E_{\text{H}_2\text{O}_2/\text{H}_2\text{O}}$ (1.78 V), it indicates that these CMPs have opportune energy band structures that are thermodynamically satisfying for both of the reduction of O_2 to generate H_2O_2 and the oxidation of H_2O by H_2O to generate H_2O_2 .

To investigate the behaviours of photogenerated charge carriers, we performed photoluminescence (PL) and time-resolved photoluminescence spectroscopy (TRPL) for the samples. Comparing with Ph-CMP, the PL intensity of Th-CMP is lower, indicating the suppression of photogenerated electron-hole pairs recombination (**Figure S13**). From TRPL (**Fig. 3d**), the average lifetime of Th-CMP (0.61 ns) is significantly lower than that of Ph-CMP (2.23 ns), manifesting rapid separation and transportation of photogenerated carriers in Th-CMP [33]. To better understand the charge transportation process between Th-CMP and Ph-CMP, we further measured the electrochemical impedance spectrum (EIS) and transient photocurrent responses of the photocatalysts. As shown in Nyquist plots in **Fig. 3e**, the radius of Th-CMP is smaller than that of Ph-CMP, indicating that it possesses weaker resistance to interfacial charge transfer along with faster transfer rate, suggesting that the introduction of thiophene group that donates electrons can effectively accelerate the interfacial charge transfer [34]. As shown in **Fig. 3f**, Th-CMP exhibited a higher photocurrent density than Ph-CMP under visible light irradiation, indicating that the introduction of thiophene group promotes the photogenerated electron-hole pairs separation. Similarly, Fu-CMP has the smallest Nyquist radius, stronger photocurrent response, and smallest average lifetime compared to Ph-CMP. It is

shown that the introduction of furan ring can promote carrier separation (**Figure S14**). During the detection of $^1\text{O}_2$, the absorbance of Th-CMP at 282 nm remained almost constant with increasing light time, indicating that the carrier separation efficiency of Th-CMP was higher than that of Ph-CMP (**Figure S15**). As a result, the introduction of the electron-giving thiophene group can promote the separation of photo-generated carriers and accelerate the interfacial charge transfer, thus facilitating the photocatalytic H_2O_2 generation.

3.3. Photocatalytic H_2O_2 evolution

The experiments pertaining to photocatalytic H_2O_2 production were initially conducted in pure water and air under visible light irradiation and without the addition of any sacrificial agent. As depicted in **Fig. 4a** and **Figure S16**, the concentration of H_2O_2 produced by Pyridyl CMP photocatalysts gradually increased with extended light exposure time. Th-CMP reached 570 μM at 40 min, which was 10 times higher than that of Ph-CMP. The variance in photocatalytic activity could be attributed to the incorporation of the electron-donating thiophene group. To investigate whether the introduction of thiophene ring can inhibit the decomposition of H_2O_2 , we performed time-dependent H_2O_2 decomposition experiments in Th-CMP under argon atmosphere. As shown in **Figure S17**, Th-CMP promotes H_2O_2 generation while inhibiting H_2O_2 decomposition. As shown in **Fig. 4b**, Th-CMP exhibited the capability to catalyze H_2O_2 production up to 1972 μM over 4 h. And the FT-IR spectra of Th-CMP did not change after a long time of photocatalytic generation of H_2O_2 , indicating that Th-CMP has a good chemical stability (**Figure S18**). The elevated catalytic activity of Th-CMP is ascribable to the efficient separation and transportation of charge carriers.

The wavelength-dependent photocatalytic H_2O_2 generation demonstrated a correlation between the H_2O_2 generation and the UV-vis DRS spectra of Th-CMP. The apparent quantum efficiency at 450 nm was determined as 2.78% (**Fig. 4c**). In addition, stability tests of Th-CMP were conducted in identical reaction conditions with the presence of

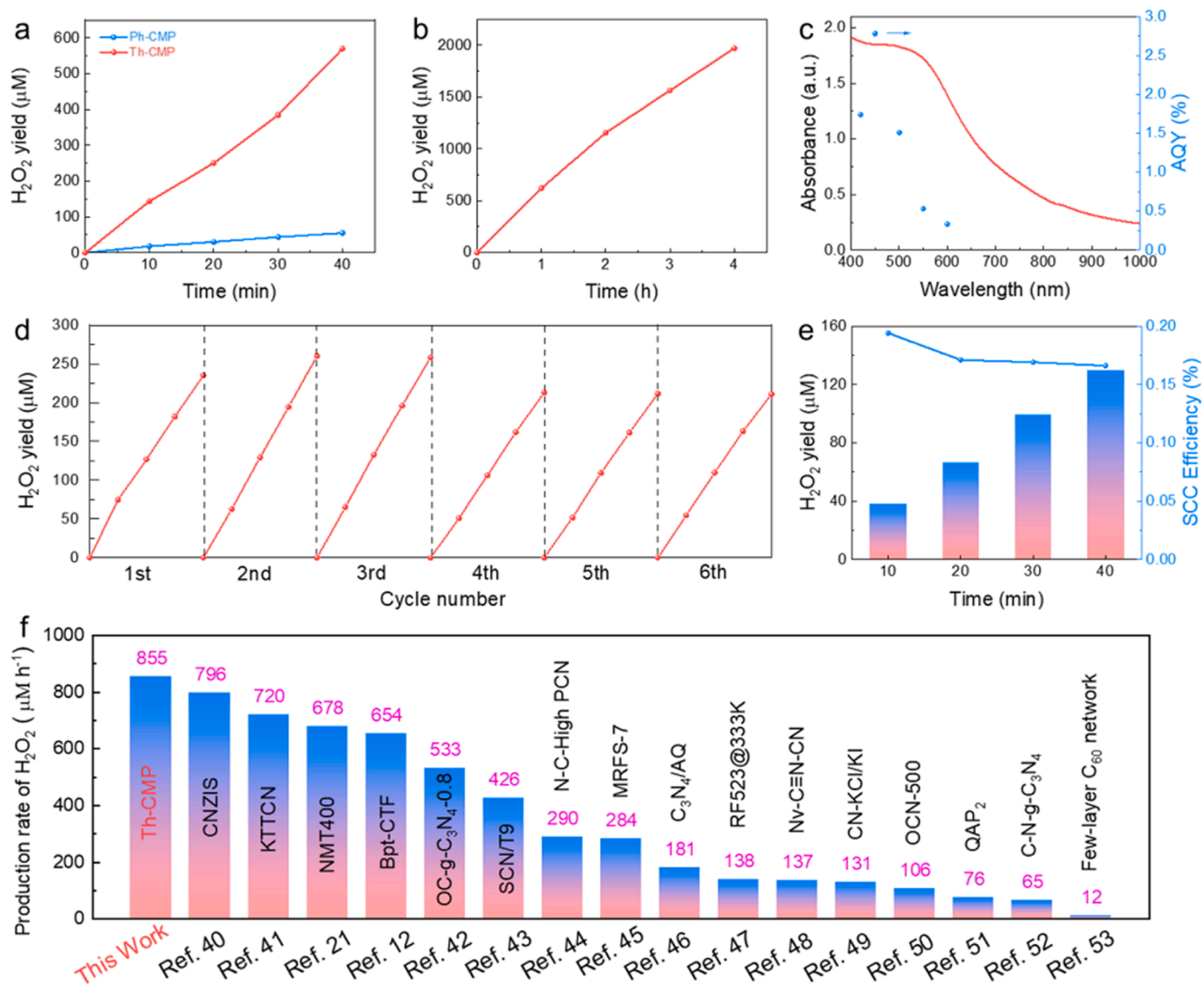


Fig. 4. Photocatalytic H₂O₂ evolution. a) Photocatalytic performance of Ph-CMP and Th-CMP for H₂O₂ production from H₂O and air. Conditions: $\lambda > 400$ nm, 100 mW cm⁻², catalyst (5 mg), water (10 mL). b) Photocatalytic yield of H₂O₂ over Th-CMP during a 4 h-duration. Conditions: $\lambda > 400$ nm, 100 mW cm⁻², catalyst (5 mg), water (10 mL). c) Apparent quantum yield of Th-CMP. Conditions: catalyst (50 mg), water (100 mL). d) Stability tests of Th-CMP for H₂O₂ production under the irradiation of visible light. Conditions: 100 mW cm⁻², catalyst (50 mg), water (100 mL). e) Solar-to-chemical conversion efficiency of Th-CMP under full spectrum irradiation. Conditions: 100 mW cm⁻², catalyst (250 mg), water (100 mL). f) Performance comparison of Th-CMP with previously reported photocatalysts [35–48].

water and air. After six repeated cycles, no significant deterioration in H₂O₂ production was observed (Fig. 4d), indicating that Th-CMP exhibits good stability for photocatalytic reactions. In Figure S19, the production of H₂O₂ gradually increased with the increase in the photocatalyst loading, and the H₂O₂ yield reached an optimal level of 1559 μM with 25 mg of loading after photo-irradiation of 40 min. It is worth noting that the H₂O₂ concentration decreased as the loading of Th-CMP was further increased to 30 mg. This is a typical phenomenon attributed to the excessive suspension concentration causing increased light scattering, leading to reduced light penetration capability [32]. Under optimal reaction conditions, Th-CMP has a higher SCC efficiency than Ph-CMP, which can reach 0.17%, surpassing the natural photosynthesis efficiency of plants (0.1%) [49] (Fig. 4e and Figure S20). Fig. 4f shows that Th-CMP has better photocatalytic H₂O₂ activity than most of the amorphous organic polymers reported in the literature [35–48].

3.4. Proposed mechanism for H₂O₂ production

Firstly, the photocatalytic generation of H₂O₂ was carried out in argon and pure water. As shown in Figure S21, the yield of H₂O₂ was 36 μM at 40 min of visible light irradiation, indicating that the photocatalytic generation of H₂O₂ has both the oxygen reduction pathway and the water oxidation pathway, and the oxygen reduction pathway plays a dominant role. The generation of ·O₂ under visible light irradiation was substantiated by the characterized reaction involving nitroblue tetrazolium (NBT) [3,50] (Figure S22). Th-CMP exhibited a photocatalytic yield of ·O₂ at 1.93×10^{-5} mol L⁻¹, notably surpassing that of Ph-CMP (Fig. 5a). On the other hand, the photocatalytic yield of ·OH over Th-CMP was determined from the characteristic reaction with benzene dicarboxylic acid as 7.81×10^{-8} mol L⁻¹. Notably, this concentration was significantly lower than that of ·O₂ and deemed negligible (Figure S23 and Fig. 5b). To elucidate the mechanism underlying the photocatalytic generation of H₂O₂ over Ph-CMP and Th-CMP, we performed a series of active species capture experiments using

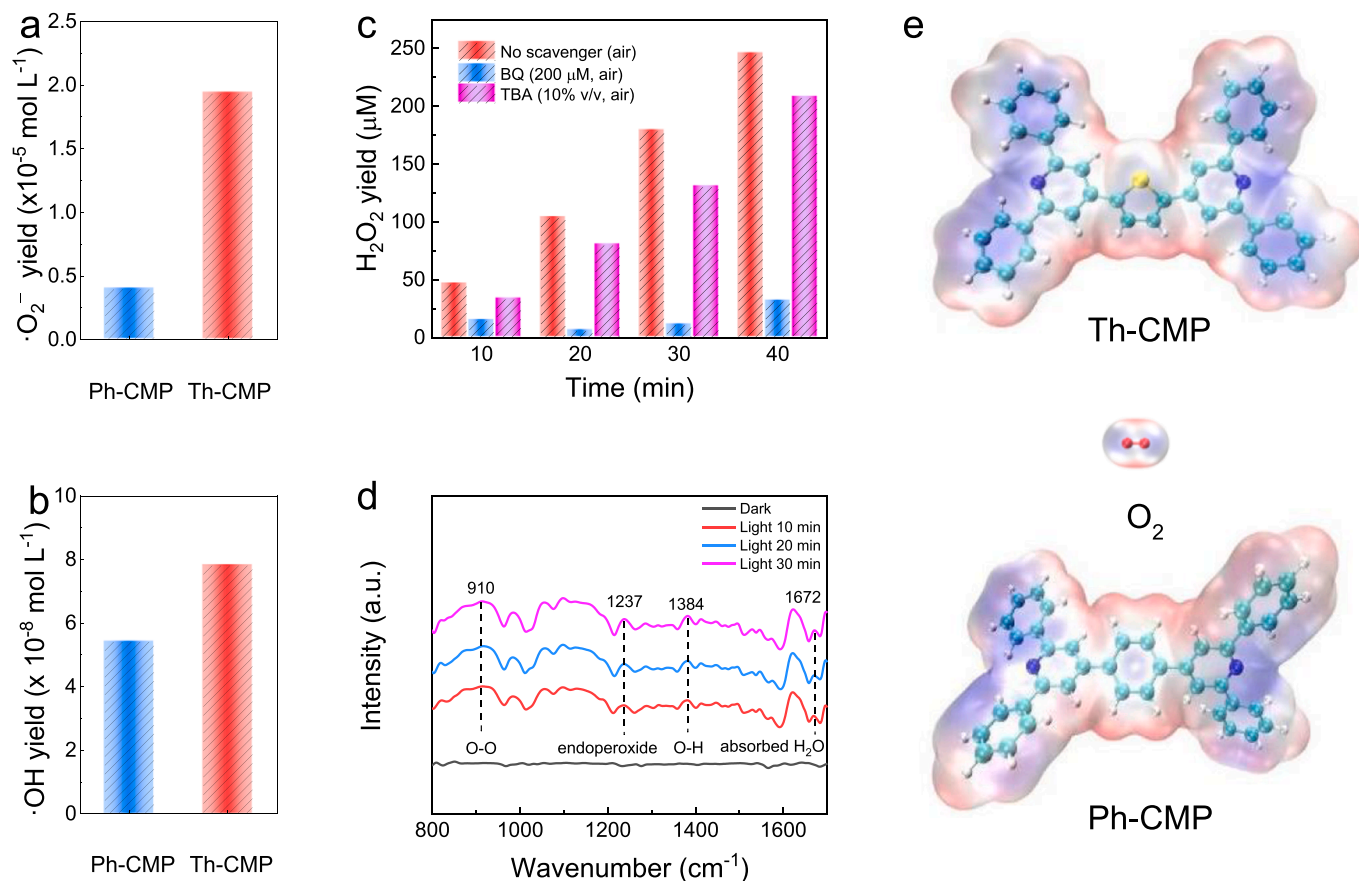


Fig. 5. Proposed mechanism for photocatalytic H_2O_2 production. a) Photocatalytic yield of $\cdot\text{O}_2^-$ over Th-CMP detected by NBT method. b) Photocatalytic yield of $\cdot\text{OH}$ over Th-CMP using terephthalic acid method. c) The yield of H_2O_2 over Th-CMP in the presence of p-benzoquinone (200 μM , as $\cdot\text{O}_2^-$ scavenger) and tert-butanol (10% v/v, as $\cdot\text{OH}$ scavenger). d) In-situ FT-IR spectra of Th-CMP for photocatalytic H_2O_2 production. e) Optimized geometries and electrostatic surface potential (ESP) of Th-CMP, Ph-CMP, and O_2 model systems. Red and blue colors indicate electron-deficient and electron-rich regions, respectively.

p-benzoquinone and tert-butanol as the scavengers for $\cdot\text{O}_2^-$ and $\cdot\text{OH}$, respectively [51]. The removal of $\cdot\text{O}_2^-$ resulted in nearly constant H_2O_2 generation yields for both CMPs as light exposure time increased, suggesting the decisive role of oxygen reduction reaction (ORR) in this photocatalytic system. Contrarily, in the presence of tert-butanol, the H_2O_2 yield exhibited minimal reduction compared to the system without scavenger, indicating that $\cdot\text{OH}$ played a negligible role in H_2O_2 generation (Fig. 5c and Figure S24). The findings from rotating disk electrode (RDE) experiments revealed that the average electron transfer numbers for Ph-CMP and Th-CMP were 2.17 and 1.62, respectively (Figure S25).

To further unveil the process of all-reactive photosynthesis of H_2O_2 catalyzed by Ph-CMP and Th-CMP, we performed in situ Fourier transform infrared spectroscopy (in-situ FT-IR) measurements to probe the photocatalytic mechanism. Fig. 5d shows the in-situ FT-IR spectra of Th-CMP over time under visible light irradiation in the presence of O_2 saturation with water vapor. After system equilibration was achieved, we observed that the vibrations of O-O (910 cm^{-1}), O-H (1384 cm^{-1}), and endoperoxide (1237 cm^{-1}) in Th-CMP were strengthened with extended light irradiation time. In addition, peaks at 1672 cm^{-1} and 3540 cm^{-1} were attributed to adsorbed H_2O [26,51,52] (Figure S26). These findings further demonstrated the mechanism of H_2O_2 catalyzed by Th-CMP involves a synergistic interplay of two-step one-electron ORR and one-step two-electron water oxidation reaction (WOR). Similar peaks emerged in the in-situ FT-IR spectra of Ph-CMP and Fu-CMP, suggesting that the prepared CMPs are also synergized by a two-step one-electron ORR and one-step two-electron WOR to generate H_2O_2 (Figure S27 and Figure S28).

To comprehend the catalytic mechanism of H_2O_2 generation over our developed photocatalysts, we performed density-functional theory

(DFT) calculations on model systems of Ph-CMP and Th-CMP [53]. As shown in Fig. 5e, we optimized the geometries of both models without any constraints and computed the electrostatic surface potential. The electron-deficient and electron-rich regions are indicated by red and blue, respectively. In Th-CMP, the electron-rich regions are concentrated at pyridine and thiophene rings, which we hypothesize to serve as active sites for photocatalytic H_2O_2 generation. To understand the photochemical processes in the catalytic reaction, we computed the frontier molecular orbitals, specifically the highest occupied molecular orbital (HOMO) and the lowest unoccupied molecular orbital (LUMO), and HOMO-LUMO energy gap (ΔE). As shown in Figure S29, the ΔE for O_2 adsorption by thiophene and pyridine of Th-CMP was 3.81 eV and 4.73 eV, respectively. The smaller the energy gap indicates that electrons are more likely to undergo electron leaps. This suggests that thiophene is more reactive in adsorbing O_2 compared to pyridine. Therefore, we hypothesized that thiophene acts as an O_2 reduction active site. In addition, as depicted in Fig. 6a, the ΔE of Th-CMP is smaller ($3.81 \text{ eV} < 4.08 \text{ eV}$) compared to that of Ph-CMP, indicating greater reactivity favouring the photocatalytic reaction. This indicates that the introduction of thiophene can effectively narrow the electron-leap gap of Th-CMP, rendering it more favorable for photocatalytic H_2O_2 generation from H_2O and air than Ph-CMP.

From Fig. 6b and Fig. 6c, for Ph-CMP, the HOMO orbitals are predominantly distributed in the pyridine ring ($\text{C}=\text{C}$), suggesting that the pyridine ring facilitates the catalytic process. The contribution of the LUMO orbitals is primarily stemmed from adsorbed O_2 . In instances where O_2 is adsorbed by Ph-CMP, photocatalytic contributions are mainly due to electron leaps from the HOMO, HOMO-10, HOMO-12, and HOMO-13 orbitals to the LUMO and LUMO+1 orbitals. For Th-

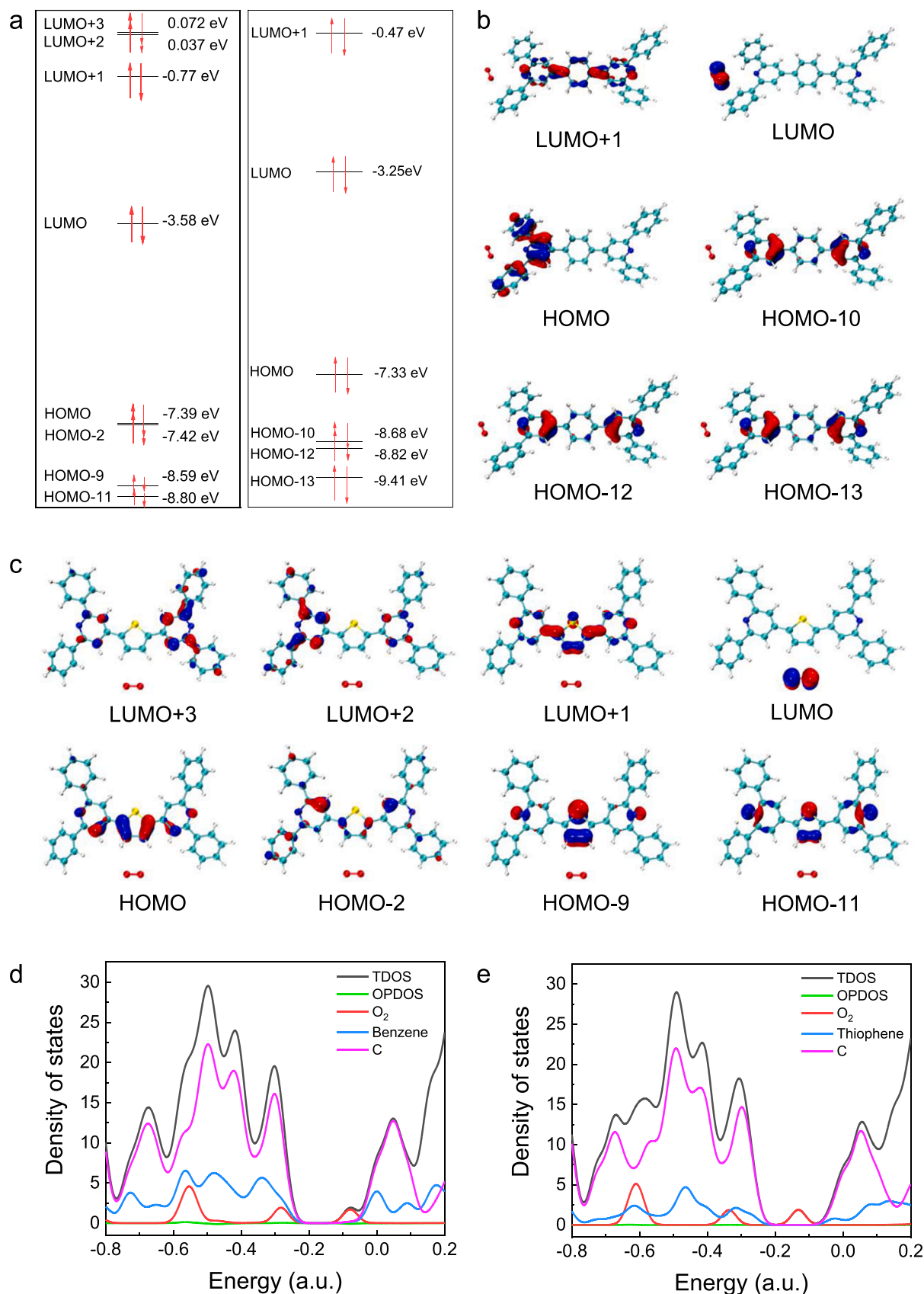


Fig. 6. Theoretical calculations. a) Calculated at the theoretical level of cam-B3LYP/6-31 G(d)-GD3BJ. (left: Th-CMP and right: Ph-CMP). b) Distribution of the HOMO and LUMO for the Ph-CMP model system, as well as the distributions of LUMO+ 1, HOMO-10, HOMO-12, and HOMO-13. c) Distribution of the HOMO and LUMO for the Th-CMP model system, as well as LUMO+ 3, LUMO+ 2, LUMO+ 1, HOMO-2, HOMO-9, and HOMO-11. d) Total density of states (TDOS) and partial density of states (PDOS) for O₂, benzene, and carbon atoms for the Ph-CMP model system. e) TDOS and PDOS for O₂, thiophene, and carbon atoms for the Th-CMP model system.

CMP, LUMO orbitals are predominantly distributed on O₂, whereas HOMO is mainly concentrated on the C=C of the thiophene ring, indicating that the thiophene ring contributes to the catalytic transition process. For the case of O₂ adsorption by Th-CMP, the contribution mainly arises from electron leaps from the HOMO, HOMO-2, HOMO-9, HOMO-11 orbitals to the LUMO, LUMO+ 1, LUMO+ 2, LUMO+ 3 orbitals. The total density of states (TDOS) and partial density of states (PDOS) maps of the O₂ absorption state on Ph-CMP and Th-CMP are presented in Fig. 6d and Fig. 6e, respectively. In the vicinity of HOMO, the carbon atoms contribute the most to the orbitals, and the contribution of the pyridine and thiophene groups cannot be ignored. This implies the facilitation of the catalytic process by the pyridine and thiophene units, in good agreement with our experimental findings.

4. Conclusions

In summary, we have developed a novel class of pyridyl CMPs for energy band structures modulation by incorporating electron-donating five-membered heterocyclic thiophenes, leading to efficient photocatalytic production of H₂O₂ from H₂O and air. Based on our experimental findings, the introduction of thiophene ring broadened the photoresponse to visible light and facilitated the separation and migration of the charge carriers, meanwhile increasing the wettability to favor the adsorption and activation of H₂O and O₂ molecules. Remarkably, the H₂O₂ yield from visible-light-driven catalytic reaction of H₂O and air in the absence of any sacrificial agent reached 855 μM h⁻¹, which was 10 times higher than that of Ph-CMP and surpassed most of the amorphous organic polymers reported in the literature hitherto. In addition, theoretical calculations divulge that the HOMO orbitals are mainly distributed on the thiophene ring of Th-CMP, suggesting that the introduction of the five-membered heterocyclic thiophene greatly promotes the generation of H₂O₂. All in all, the pyridyl CMP developed in this work provides some insights into the development of organic polymer photocatalysts for the production of H₂O₂ with enormous potential to be applied in industrial scale.

CRediT authorship contribution statement

Shi Zhonglian: Formal analysis. **Wang Li:** Formal analysis, Data curation. **Lv Minghui:** Formal analysis. **Li Mingjin:** Formal analysis. **Wang Long:** Supervision. **Xu Run:** Formal analysis. **Shen Yi:** Formal analysis. **Wang Qiao:** Formal analysis. **Ye Liqun:** Writing – review & editing, Supervision, Funding acquisition, Formal analysis, Conceptualization. **Yang Chen:** Formal analysis. **Zheng Yong:** Writing – review & editing, Supervision, Funding acquisition, Conceptualization. **Kong Xin Ying:** Writing – review & editing. **Gao Tao:** Writing – original draft, Formal analysis, Data curation.

Declaration of Competing Interest

The authors declare that they have no known competing financial interests or personal relationships that could have appeared to influence the work reported in this paper.

Data Availability

Data will be made available on request.

Acknowledgments

This work is supported by the National Natural Science Foundation of China (51872147), Hubei Provincial Natural Science Foundation of China (No. 2022CFB820, 2022CFA065), and the 111 Project (D20015).

Appendix A. Supporting information

Supplementary data associated with this article can be found in the online version at doi:10.1016/j.apcatb.2024.123761.

References

- [1] L. Li, L. Xu, Z. Hu, J.C. Yu, Enhanced mass transfer of oxygen through a gas-liquid-solid interface for photocatalytic hydrogen peroxide production, *Adv. Funct. Mater.* 31 (2021) 2106120.
- [2] L. Liu, M.Y. Gao, H. Yang, X. Wang, X. Li, A.I. Cooper, Linear conjugated polymers for solar-driven hydrogen peroxide production: the importance of catalyst stability, *J. Am. Chem. Soc.* 143 (2021) 19287–19293.
- [3] H. Wang, C. Yang, F. Chen, G. Zheng, Q. Han, A crystalline partially fluorinated triazine covalent organic framework for efficient photosynthesis of hydrogen peroxide, *Angew. Chem. Int. Ed.* 61 (2022) e202202328.
- [4] H. Cheng, J. Cheng, L. Wang, H. Xu, Reaction pathways toward sustainable photosynthesis of hydrogen peroxide by polymer photocatalysts, *Chem. Mater.* 34 (2022) 4259–4273.
- [5] S. Wang, B. Cai, H. Tian, Efficient generation of hydrogen peroxide and formate by an organic polymer dots photocatalyst in alkaline conditions, *Angew. Chem. Int. Ed.* 61 (2022) e202202733.
- [6] W. Li, Z. Zhao, W. Hu, Q. Cheng, L. Yang, Z. Hu, Y.A. Liu, K. Wen, H. Yang, Design of thiazolo[5,4-d]thiazole-bridged ionic covalent organic polymer for highly selective oxygen reduction to H₂O₂, *Chem. Mater.* 32 (2020) 8553–8560.
- [7] Z. Jin, Y. Liu, L. Wang, C. Wang, Z. Wu, Q. Zhu, L. Wang, F.S. Xiao, Direct synthesis of pure aqueous H₂O₂ solution within aluminosilicate zeolite crystals, *ACS Catal.* 11 (2021) 1946–1951.
- [8] W. Liu, P. Wang, J. Chen, X. Gao, H. Che, B. Liu, Y. Ao, Unraveling the mechanism on ultrahigh efficiency photocatalytic H₂O₂ generation for dual-heteroatom incorporated polymeric carbon nitride, *Adv. Funct. Mater.* 32 (2022) 2205119.
- [9] Z. Teng, Q. Zhang, H. Yang, K. Kato, W. Yang, Y.R. Lu, S. Liu, C. Wang, A. Yamakata, C. Su, B. Liu, T. Ohno, Atomically dispersed antimony on carbon nitride for the artificial photosynthesis of hydrogen peroxide, *Nat. Catal.* 4 (2021) 374–384.
- [10] D. Chen, W. Chen, Y. Wu, L. Wang, X. Wu, H. Xu, L. Chen, Covalent organic frameworks containing dual O₂ reduction centers for overall photosynthetic hydrogen peroxide production, *Angew. Chem. Int. Ed.* 62 (2023) e202217479.
- [11] C. Krishnaraj, H. Sekhar Jena, L. Bourda, A. Laemont, P. Pachfule, J. Roeser, C. V. Chandran, S. Borgmans, S.M.J. Rogge, K. Leus, C.V. Stevens, J.A. Martens, V. Van Speybroeck, E. Breynaert, A. Thomas, P. Van Der Voort, Strongly reducing (diarylamino) benzene-based covalent organic framework for metal-free visible light photocatalytic H₂O₂ generation, *J. Am. Chem. Soc.* 142 (2020) 20107–20116.
- [12] C. Wu, Z. Teng, C. Yang, F. Chen, H.B. Yang, L. Wang, H. Xu, B. Liu, G. Zheng, Q. Han, Polarization engineering of covalent triazine frameworks for highly efficient photosynthesis of hydrogen peroxide from molecular oxygen and water, *Adv. Mater.* 34 (2022) 2110266.
- [13] C. Zhao, X. Wang, Y. Yin, W. Tian, G. Zeng, H. Li, S. Ye, L. Wu, J. Liu, Molecular level modulation of anthraquinone-containing resorcinol-formaldehyde resin photocatalysts for H₂O₂ production with exceeding 1.2% efficiency, *Angew. Chem. Int. Ed.* 62 (2023) e202218318.
- [14] L. Yuan, C. Zhang, J. Wang, C. Liu, C. Yu, Mesoporous resin nanobowls with optimized donor-acceptor conjugation for highly efficient photocatalytic hydrogen peroxide production, *Nano Res* 14 (2021) 3267–3273.
- [15] X. Gao, C. Shu, C. Zhang, W. Ma, S.B. Ren, F. Wang, Y. Chen, J.H. Zeng, J.X. Jiang, Substituent effect of conjugated microporous polymers on the photocatalytic hydrogen evolution activity, *J. Mater. Chem. A* 8 (2020) 2404–2411.
- [16] R.S. Sprick, Y. Bai, A.A.Y. Guilbert, M. Zbiri, C.M. Aitchison, L. Wilbraham, Y. Yan, D.J. Woods, M.A. Zwijnenburg, A.I. Cooper, Photocatalytic hydrogen evolution from water using fluorene and dibenzothiophene sulfone-conjugated microporous and linear polymers, *Chem. Mater.* 31 (2019) 305–313.
- [17] G. Zhang, W. Ou, J. Wang, Y. Xu, D. Xu, T. Sun, S. Xiao, M. Wang, H. Li, W. Chen, C. Su, Stable, carrier separation tailorable conjugated microporous polymers as a platform for highly efficient photocatalytic H₂ evolution, *Appl. Catal. B* 245 (2019) 114–121.
- [18] C. Zhang, Y. Qiao, P. Xiong, W. Ma, P. Bai, X. Wang, Q. Li, J. Zhao, Y. Xu, Y. Chen, J.H. Zeng, F. Wang, Y. Xu, J.X. Jiang, Conjugated microporous polymers with tunable electronic structure for high-performance potassium-ion batteries, *ACS Nano* 13 (2019) 745–754.
- [19] L. Ma, Y. Liu, Y. Liu, S. Jiang, P. Li, Y. Hao, P. Shao, A. Yin, X. Feng, B. Wang, Ferrocene-linkage-facilitated charge separation in conjugated microporous polymers, *Angew. Chem. Int. Ed.* 58 (2019) 4221–4226.
- [20] F. Yu, Z. Zhu, S. Wang, J. Wang, Z. Xu, F. Song, Z. Dong, Z. Zhang, Novel donor-acceptor-acceptor ternary conjugated microporous polymers with boosting forward charge separation and suppressing backward charge recombination for photocatalytic reduction of uranium (VI), *Appl. Catal. B* 301 (2022) 120819.
- [21] C. Yang, S. Wan, B. Zhu, J. Yu, S. Cao, Calcination-regulated microstructures of donor-acceptor polymers towards enhanced and stable photocatalytic H₂O₂ production in pure water, *Angew. Chem. Int. Ed.* 61 (2022) e202208438.
- [22] M. Liu, K. Yang, Z. Li, E. Fan, H. Fu, L. Zhang, Y. Zhang, Z. Zheng, The O/S heteroatom effects of covalent triazine frameworks for photocatalytic hydrogen evolution, *ChemComm* 58 (2022) 92–95.

- [23] W. Zhang, Z. Deng, J. Deng, C.T. Au, Y. Liao, H. Yang, Q. Liu, Regulating the exciton binding energy of covalent triazine frameworks for enhancing photocatalysis, *J. Mater. Chem. A* 10 (2022) 22419–22427.
- [24] Y. Liu, J. Wu, F. Wang, Dibenzo[thiophene-S,S-dioxide]-containing conjugated polymer with hydrogen evolution rate up to 147 mmol g⁻¹ h⁻¹, *Appl. Catal. B* 307 (2022) 121144.
- [25] Z. Cheng, L. Wang, Y. He, X. Chen, X. Wu, H. Xu, Y. Liao, M. Zhu, Rapid metal-free synthesis of pyridyl-functionalized conjugated microporous polymers for visible-light-driven water splitting, *Polym. Chem.* 11 (2020) 3393–3397.
- [26] M. Kou, Y. Wang, Y. Xu, L. Ye, Y. Huang, B. Jia, H. Li, J. Ren, Y. Deng, J. Chen, Y. Zhou, K. Lei, L. Wang, W. Liu, H. Huang, T. Ma, Molecularly engineered covalent organic frameworks for hydrogen peroxide photosynthesis, *Angew. Chem. Int. Ed.* 61 (2022) e202200413.
- [27] Z. Cheng, Y. He, C. Yang, N. Meng, Y. Liao, Metal-free synthesis of pyridyl conjugated microporous polymers with tunable bandgaps for efficient visible-light-driven hydrogen evolution, *Chin. Chem. Lett.* 34 (2022) 107440.
- [28] S. Ghasimi, S.A. Bretschneider, W. Huang, K. Landfester, K.A.I. Zhang, A conjugated microporous polymer for palladium-free, visible light-promoted photocatalytic stille-type coupling reactions, *Adv. Sci.* 4 (2017) 1700101.
- [29] Z. You, Z. Zhao, Q. Zhang, C. Zhang, X. Long, D. Li, Y. Xia, Organic heterocyclic strategy for precisely regulating electronic state of palladium interface to boost alcohol oxidation, *Adv. Funct. Mater.* 33 (2023) 2210877.
- [30] Z. Gu, J. Wang, Z. Shan, M. Wu, T. Liu, L. Song, G. Wang, X. Ju, J. Su, G. Zhang, Modulating electronic structure of triazine-based covalent organic frameworks for photocatalytic organic transformations, *J. Mater. Chem. A* 10 (2022) 17624–17632.
- [31] X. Zhong, Q. Ling, Z. Ren, B. Hu, Immobilization of U(VI) onto covalent organic frameworks with the different periodic structure by photocatalytic reduction, *Appl. Catal. B* 326 (2023) 122398.
- [32] Y. Zhang, C. Pan, G. Bian, J. Xu, Y. Dong, Y. Zhang, Y. Lou, W. Liu, Y. Zhu, H₂O₂ generation from O₂ and H₂O on a near-infrared absorbing porphyrin supramolecular photocatalyst, *Nat. Energy* 8 (2023) 361–371.
- [33] X. Xu, R. Sa, W. Huang, Y. Sui, W. Chen, G. Zhou, X. Li, Y. Li, H. Zhong, Conjugated organic polymers with anthraquinone redox centers for efficient photocatalytic hydrogen peroxide production from water and oxygen under visible light irradiation without any additives, *ACS Catal.* 12 (2022) 12954–12963.
- [34] Z. Zhou, M. Sun, Y. Zhu, P. Li, Y. Zhang, M. Wang, Y. Shen, A thioether-decorated triazine-based covalent organic framework towards overall H₂O₂ photosynthesis without sacrificial agents, *Appl. Catal. B* 334 (2023) 122862.
- [35] K. Zhang, M. Dan, J. Yang, F. Wu, L. Wang, H. Tang, Z.Q. Liu, Surface energy mediated sulfur vacancy of ZnIn₂S₄ atomic layers for photocatalytic H₂O₂ production, *Adv. Funct. Mater.* 33 (2023) 2302964.
- [36] J. Zhang, C. Yu, J. Lang, Y. Zhou, B. Zhou, Y.H. Hu, M. Long, Modulation of lewis acidic-basic sites for efficient photocatalytic H₂O₂ production over potassium intercalated tri-s-triazine materials, *Appl. Catal. B* 277 (2020) 119225.
- [37] Q. Hu, Y. Dong, K. Ma, X. Meng, Y. Ding, Amidation crosslinking of polymeric carbon nitride for boosting photocatalytic hydrogen peroxide production, *J. Catal.* 413 (2022) 321–330.
- [38] Z. Jiang, Q. Long, B. Cheng, R. He, L. Wang, 3D ordered macroporous sulfur-doped g-C₃N₄/TiO₂ S-scheme photocatalysts for efficient H₂O₂ production in pure water, *J. Mater. Sci. Technol.* 162 (2023) 1–10.
- [39] Y. Ma, H. Sun, Q. Wang, L. Sun, Z. Liu, Y. Xie, Q. Zhang, C. Su, D. Fan, Driving hydrogen peroxide artificial photosynthesis and utilization for emerging contaminants removal by cyanided polymeric carbon nitride, *Appl. Catal. B* 335 (2023) 122878.
- [40] Q. Tian, L. Jing, S. Ye, J. Liu, R. Chen, C.A.H. Price, F. Fan, J. Liu, Nanospatial charge modulation of monodispersed polymeric microsphere photocatalysts for exceptional hydrogen peroxide production, *Small* 17 (2021) 2103224.
- [41] H. Kim, Y. Choi, S. Hu, W. Choi, J.H. Kim, Photocatalytic hydrogen peroxide production by anthraquinone-augmented polymeric carbon nitride, *Appl. Catal. B* 229 (2018) 121–129.
- [42] Y. Shiraishi, T. Takii, T. Hagi, S. Mori, Y. Kofuji, Y. Kitagawa, S. Tanaka, S. Ichikawa, T. Hirai, Resorcinol-formaldehyde resins as metal-free semiconductor photocatalysts for solar-to-hydrogen peroxide energy conversion, *Nat. Mater.* 18 (2019) 985–993.
- [43] X. Zhang, P. Ma, C. Wang, L. Gan, X. Chen, P. Zhang, Y. Wang, H. Li, L. Wang, X. Zhou, K. Zheng, Unraveling the dual defect sites in graphite carbon nitride for ultra-high photocatalytic H₂O₂ evolution, *Energy Environ. Sci.* 15 (2022) 830–842.
- [44] L.L. Liu, F. Chen, J.H. Wu, J.J. Chen, H.Q. Yu, Synergy of crystallinity modulation and intercalation engineering in carbon nitride for boosted H₂O₂ photosynthesis, *Proc. Natl. Acad. Sci. U. S. A.* 120 (2023) e2215305120.
- [45] Z. Wei, M. Liu, Z. Zhang, W. Yao, H. Tan, Y. Zhu, Efficient visible-light-driven selective oxygen reduction to hydrogen peroxide by oxygen-enriched graphitic carbon nitride polymers, *Energy Environ. Sci.* 11 (2018) 2581–2589.
- [46] B. Sheng, Y. Xie, Q. Zhao, H. Sheng, J. Zhao, Proton reservoir in polymer photocatalysts for the superior H₂O₂ photosynthesis, *Energy Environ. Sci.* 16 (2023) 4612–4619.
- [47] Y. Fu, C. Liu, M. Zhang, C. Zhu, H. Li, H. Wang, Y. Song, H. Huang, Y. Liu, Z. Kang, Photocatalytic H₂O₂ and H₂ generation from living *Chlorella vulgaris* and carbon micro particle comodified g-C₃N₄, *Adv. Energy Mater.* 8 (2018) 1802525.
- [48] T. Wang, L. Zhang, J. Wu, M. Chen, S. Yang, Y. Lu, P. Du, Few-layer fullerene network for photocatalytic pure water splitting into H₂ and H₂O₂, *Angew. Chem. Int. Ed.* 62 (2023) e202311352.
- [49] H. Tan, P. Zhou, M. Liu, Q. Zhang, F. Liu, H. Guo, Y. Zhou, Y. Chen, L. Zeng, L. Gu, Z. Zheng, M. Tong, S. Guo, Photocatalysis of water into hydrogen peroxide over an atomic Ga-N₅ site, *Nat. Synth.* 2 (2023) 557–563.
- [50] Y. Liu, W.K. Han, W. Chi, Y. Mao, Y. Jiang, X. Yan, Z.G. Gu, Substoichiometric covalent organic frameworks with uncondensed aldehyde for highly efficient hydrogen peroxide photosynthesis in pure water, *Appl. Catal. B* 331 (2023) 122691.
- [51] J. Sun, H. Sekhar Jena, C. Krishnaraj, K. Singh Rawat, S. Abednatanzi, J. Chakraborty, A. Laemont, W. Liu, H. Chen, Y.Y. Liu, K. Leus, H. Vrielinck, V. Van Speybroeck, P. Van Der Voort, Pyrene-based covalent organic frameworks for photocatalytic hydrogen peroxide production, *Angew. Chem. Int. Ed.* 62 (2023) e202216719.
- [52] J.N. Chang, Q. Li, J.W. Shi, M. Zhang, L. Zhang, S. Li, Y. Chen, S.L. Li, Y.Q. Lan, Oxidation-reduction molecular junction covalent organic frameworks for full reaction photosynthesis of H₂O₂, *Angew. Chem. Int. Ed.* 62 (2023) e202218868.
- [53] L. Zhai, Z. Xie, C.X. Cui, X. Yang, Q. Xu, X. Ke, M. Liu, L.B. Qu, X. Chen, L. Mi, Constructing synergistic triazine and acetylene cores in fully conjugated covalent organic frameworks for cascade photocatalytic H₂O₂ production, *Chem. Mater.* 34 (2022) 5232–5240.